applied sciences

MDPI

Article

Explainable Data-Driven Ensemble Learning Models for the Mechanical Properties Prediction of Concrete Confined by Aramid Fiber-Reinforced Polymer Wraps Using Generative Adversarial Networks

Celal Cakiroglu

Department of Civil Engineering, Turkish-German University, Istanbul 34820, Turkey; cakiroglu@tau.edu.tr

Abstract: The current study offers a data-driven methodology to predict the ultimate strain and compressive strength of concrete reinforced by aramid FRP wraps. An experimental database was collected from the literature, on which seven different machine learning (ML) models were trained. The diameter and length of the cylindrical specimens, the compressive strength of unconfined concrete, the thickness, elasticity modulus and ultimate tensile strength of the FRP wrap were used as the input features of the machine learning models, to predict the ultimate strength and strain of the specimens. The experimental dataset was further enhanced with synthetic data using the tabular generative adversarial network (TGAN) approach. The machine learning models' performances were compared to the predictions of the existing strain capacity and compressive strength prediction equations for aramid FRP-confined concrete. The accuracy of the predictive models was measured using state-of-the-art statistical metrics such as the coefficient of determination, mean absolute error and root mean squared error. On average, the machine learning models were found to perform better than the available equations in the literature. In particular, the extra trees regressor, XGBoost and K-nearest neighbors algorithms performed significantly better than the remaining algorithms, with R^2 scores greater than 0.98. Furthermore, the SHapley Additive exPlanations (SHAP) method and individual conditional expectation (ICE) plots were used to visualize the effects of various input parameters on the predicted ultimate strain and strength values. The unconfined compressive strength of concrete and the ultimate tensile strength of the FRP wrap were found to have the greatest impact on the machine learning model outputs.

Keywords: aramid fiber reinforced polymers; machine learning; compressive strength; concrete confinement; XGBoost; SHAP; TGAN

Citation: Cakiroglu, C. Explainable Data-Driven Ensemble Learning Models for the Mechanical Properties Prediction of Concrete Confined by Aramid Fiber-Reinforced Polymer Wraps Using Generative Adversarial Networks. *Appl. Sci.* **2023**, *13*, 11991. https://doi.org/10.3390/app132111991

Academic Editors: Ki-Bong Park and Xiaoyong Wang

Received: 29 September 2023
Revised: 27 October 2023
Accepted: 31 October 2023
Published: 2 November 2023

1. Introduction

Concrete confinement using fiber-reinforced polymer (FRP) jackets is widely applied in structural retrofitting. FRP confinement can strengthen reinforced concrete columns by increasing the axial load carrying capacity, the shear and flexural strengths and the performance under seismic loads [1]. Their resistance to corrosion, light weight and ease of construction are further benefits of using FRP materials instead of concrete or steel jackets [2]. As reinforcement materials, carbon fibers are mostly used. However, carbon fibers are known to have less ductility compared to materials such as steel or glass. Aramid fiber reinforcement has attracted attention in recent years, due to its favorable combination of ductility and strength. It is reported that aramid fibers have better strength properties than glass fibers and better ductility than carbon fibers [3]. The performance of FRP-wrapped concrete columns and composite structures in general, such as laminated composite plates, has been extensively studied under various loading conditions. Shih et al. [4] investigated the application of aramid fiber-reinforced polymers (AFRP) in

soft body armor systems. The impact resistance, energy absorption and deformation properties of these systems have been tested using ballistics tests. It was reported that polyurea elastomer processing of Kevlar plates reduces the weight and thickness of multilayered soft body armors and improves the impact resistance. Alkhatib et al. [5] compared the performances of Kevlar, date palm, carbon, and hybrid fibers used in armor plates in terms of energy absorption with finite element analysis. The hybrid composite plates were found to perform best in terms of energy absorption. The usage of shear thickening fluid impregnation to enhance the penetration resistance of AFRP armor plates was proposed by Lee et al. [6]. The addition of shear thickening fluid was shown to improve the flexibility, reduce the thickness and enhance the impact resistance of the armor plates. Wang et al. [7] tested the impact resistance, flexibility and single yarn pull-out resistance of aramid fabrics impregnated with shear thickening fluid and adhesive polyurethane. The aramid fabrics impregnated with both shear thickening fluid and polyurethane were shown to perform better in terms of impact resistance. Another study with hybrid composites was carried out by Meliande et al. [8], who demonstrated the application of natural curaua fibers, in combination with aramid fibers in laminated composite plates. Increasing the number of curaua-reinforced layers was shown to reduce the flexural strength, energy absorption, and stiffness. Fiber-reinforced polymers have also found applications in the area of pile splicing. Khedmatgozar Dolati and Mehrabi [9,10] implemented FRP materials in the splicing of prestressed precast concrete piles. A new FRP-based splicing method has been proposed as an economical and corrosion-resistant splicing technique which satisfies the established design requirements.

The application of FRP wraps to increase the load-carrying capacity of reinforced concrete structures has certain advantages, such as corrosion resistance, a light weight, high stiffness and easy adaptability to the shape of the structure [11]. Choi et al. [12] investigated the effect of using FRP wire wraps on the structural behavior of concrete. The application of FRP wire wraps was found to increase the peak strength and reduce volumetric expansion. Iacobucci et al. [13] carried out experiments with full scale reinforced concrete columns with insufficient transverse steel reinforcement, retrofitted with carbon fiber- and glass fiber-reinforced polymer wraps. The specimens were tested under lateral cyclic loading. During cyclic loading, it was observed that adding more FRP layers enhances the stiffness and strength. It was also shown that deficient columns properly retrofitted with CFRP can perform better than sufficiently reinforced columns without CFRP wraps. Yang et al. [14] tested AFRP-confined concrete specimens under high strain rate compression. The effect of changing the confinement layer thicknesses was also investigated. The AFRP confinement was shown to improve the dynamic strength, ultimate strain and impact resistance of the tested specimens. Xie et al. [15] conducted axial compression experiments on square reinforced concrete columns confined with basalt FRP wraps. The basalt–FRP confinement was shown to improve the compressive strength and ductility.

It is known that FRP wraps have greater effectiveness in circular columns compared to rectangular columns. In rectangular columns, the effectiveness of confinement is limited to the areas surrounding the corners [2]. Sharma et al. [16] investigated the effect of changing the corner radius on the structural behavior of rectangular columns confined with glass fiber-reinforced polymer (GFRP) wraps. It was concluded that columns with a corner radius equal to concrete cover have better results, in terms of axial load carrying capacity, compared to columns with a corner radius less than the concrete cover. Due to the differences in the confinement of rectangular and circular columns, different sets of equations have been proposed in the literature for the prediction of the compressive strength and ultimate strain of FRP-wrapped columns with circular and rectangular cross-sections. Some of these equations do not distinguish between different fiber materials [17–20], whereas others are developed specifically for FRP wraps made of aramid fibers [21–24].

In recent years, machine learning techniques have been increasingly applied in the field of predicting the mechanical properties of concrete structures. In particular, the effects of different ingredients such as fly ash, silica, or ceramic waste powder on the com-

pressive strength of concrete have been investigated, using techniques such as ensemble machine learning, artificial neural networks and gene expression programming [25–27]. Ahmad et al. [28] investigated fly ash-based geopolymer concrete with respect to its compressive strength using the AdaBoost, bagging regressor and decision tree algorithms. The bagging regressor was found to be the most accurate among these algorithms in predicting the compressive strength. Shang et al. [29] used decision tree and AdaBoost algorithms to predict the compressive strength and splitting tensile strength of recycled coarse aggregate-based concrete. A coefficient of determination of 0.95 could be achieved from the AdaBoost algorithm. The applicability of the gene expression programming algorithm in compressive strength prediction was shown by Ahmad et al. [30] and Farooq et al. [31] for recycled aggregate concrete and high strength concrete, respectively. The splitting tensile strength of recycled aggregate-based concrete was also investigated by Amin et al. [32]. Decision tree, random forest and artificial neural network techniques were applied. It was shown that the random forest algorithm outperformed the decision tree and artificial neural network algorithms.

In this study, the performances of the equations from the literature developed for aramid fiber-reinforced polymer (AFRP)-wrapped circular columns were compared to the predictions of the machine learning (ML) algorithms. A dataset of 225 samples with circular cross-sections was collected from the literature [3,21,22,24,33–49] which can be found in Supplementary Materials (under the GitHub link https://github.com/ccakiroglu/AFRP (accessed on 27 October 2023)). A 159-sample subset of this dataset was used for the training of ML models for the prediction of ultimate strain. The experimental datasets were further enhanced using the tabular generative adversarial network (TGAN) methodology. It was shown that the currently available predictive equations in the literature can be significantly inaccurate when applied to new datasets. As an alternative approach to predictive equations, ML models were presented as a means of making accurate predictions about structural behavior. The impacts of different input features on the model predictions were quantified using the SHapley Additive exPlanations (SHAP) method, and the input features were ranked according to their impacts on the model predictions. Furthermore, the changes in the model predictions, with respect to the most impactful input features, were visualized using individual conditional expectation (ICE) plots. Due to the favorable mechanical properties of aramid fiber-reinforced polymers (AFRP), these materials are finding applications in various areas of structural engineering. Therefore, the availability of reliable and accurate prediction methods for the mechanical properties of AFRP-confined concrete structures is crucial.

The current study presents a novel approach to predicting structural behavior, with the help of explainable ensemble ML models. The effect of different parameters on the mechanical behavior of AFRP-confined concrete is visualized using the SHAP algorithm. Furthermore, an alternative approach is proposed for generating large synthetic datasets, which could be utilized to train predictive models. The study is distinctive in that it aims to prepare big datasets, with the help of tabular generative adversarial networks, for applications in the prediction of the mechanical properties of composite materials. In the case of FRP wraps, the identification of mechanical properties necessitates costly experimental procedures or finite element modelling. Therefore, generative machine learning techniques present a valuable alternative to these traditional techniques for generating large datasets. The availability of large datasets is vital for the application of ML techniques. Therefore, the study makes a significant contribution towards the adoption of ML techniques in modelling engineering systems.

2. Predictive Equations and Machine Learning Models

2.1. Predictive Equations for the Compressive Strength and Ultimate Strain

For circular columns wrapped with an AFRP jacket, the following equations in Tables 1 and 2 provide a list of some of the available predictive equations for the prediction of confined compressive strength and ultimate strain, respectively.

Table 1. Equations for the predictions of the compressive strength f_{cc}.

Model	Reference
$f_{cc} = f_{co} + 6.4\frac{f_f t_f}{D}$	Wu et al. [21]
$f_{cc} = f_{co}\left(\frac{\left(1+5.54\frac{2f_f t_f}{Df_{co}}\right)}{\sqrt{1+\frac{L-D}{353}\left(1-1.49\frac{2f_f t_f}{Df_{co}}\right)}}\right)$	Wang and Wu [22]
$f_{cc} = f_{co}\left(1 + 1.2\left(\frac{2f_f t_f}{Df_{co}}\right)^{1.25}\left(\frac{2E_f t_f}{Df_{co}}\right)^{0.37}\right)$	Djafar-Henni and Kassoul [23]
$f_{cc} = f_{co} + 6.2\frac{f_f t_f}{D}$	Lobo et al. [24]

Table 2. Equations for the predictions of the ultimate strain ε_{cu}.

Model	Reference
$\varepsilon_{cu} = \varepsilon_{co}\left(1 + 19\frac{f_f t_f}{Df_{co}}\right)$	Wu et al. [21]
$\varepsilon_{cu} = \varepsilon_{co} + 0.152\frac{f_f t_f}{Df_{co}}$	Lobo et al. [24]

In Table 1, f_{co}, f_{cc}, f_f, t_f, E_f, and D stand for the unconfined compressive strength, confined compressive strength, the ultimate tensile strength of AFRP, the total thickness of the AFRP jacket, the elastic modulus of AFRP and the diameter of the specimens, respectively. In the case of confined ultimate strain prediction, the equations in Table 2 were investigated, where ε_{cu} and ε_{co} stand for the ultimate strain of confined concrete and the axial strain of unconfined concrete at f_{co}, respectively. For the equations in Tables 1 and 2, the units of the stress variables f_{co}, f_{cc}, f_f and the elastic modulus E_f are in MPa, while the length parameters t_f and D use the unit of mm.

2.2. Training of the Machine Learning Models

The datasets used to train the machine learning (ML) models include both synthetic and real data points. Due to the differences in the availability of data points for strain and stress prediction, different datasets were used as the base dataset for the generation of synthetic data points. The base dataset for the confined compressive strength model consists of 225 data points whereas the base dataset for the ultimate strain prediction consists of 159 data points. The datasets contain information about the unconfined concrete strength (f_{co}), diameter of the circular column being tested (d), height of the column (L), ultimate tensile strength of the AFRP material (f_f), elastic modulus of the AFRP (E_f), and the thickness of the AFRP jacket (t_f) as input variables. The confined compressive strength (f_{cc}) and the ultimate strain of confined concrete (ε_{cu}) are the output variables predicted by the ML models.

Figure 1 shows the Pearson correlation between all the input features and the compressive strength of the confined concrete (f_{cc}). The Pearson correlation values between the variables are shown inside the boxes in the upper right triangle of the correlation diagram. Equation (1) illustrates the calculation of the Pearson correlation values (r_{xy}), where x and y denote two variables. An r_{xy} value close to 1 denotes strong linear proportionality between two variables, whereas an r_{xy} value close to -1 denotes strong inverse proportionality between two variables.

In the upper right triangular part of the diagram, the number of stars denotes the strength of correlation between two variables. The frequency distribution histogram of each variable is shown in the diagonal of the diagram. The lower left triangular part of the correlation diagram displays the bivariate scatter plots of the variables with regression lines. According to Figure 1, the strongest correlation in the dataset between any two variables can be observed between the confined compressive strength of concrete (f_{cc}) and the unconfined compressive strength of concrete (f_{co}), with an r_{xy} value of 0.24. The second strongest correlation is between the AFRP elastic modulus (E_f) and the ultimate tensile

strength of AFRP (f_f). On the other hand, there is a relatively strong inverse proportionality between the AFRP elastic modulus (E_f) and the total thickness of the AFRP jacket (t_f).

$$r_{xy} = \frac{n\sum_{i=1}^{n} x_i y_i - \sum_{i=1}^{n} x_i \sum_{i=1}^{n} y_i}{\sqrt{n\sum_{i=1}^{n} x_i^2 - \left(\sum_{i=1}^{n} x_i\right)^2}\sqrt{n\sum_{i=1}^{n} y_i^2 - \left(\sum_{i=1}^{n} y_i\right)^2}} \quad (1)$$

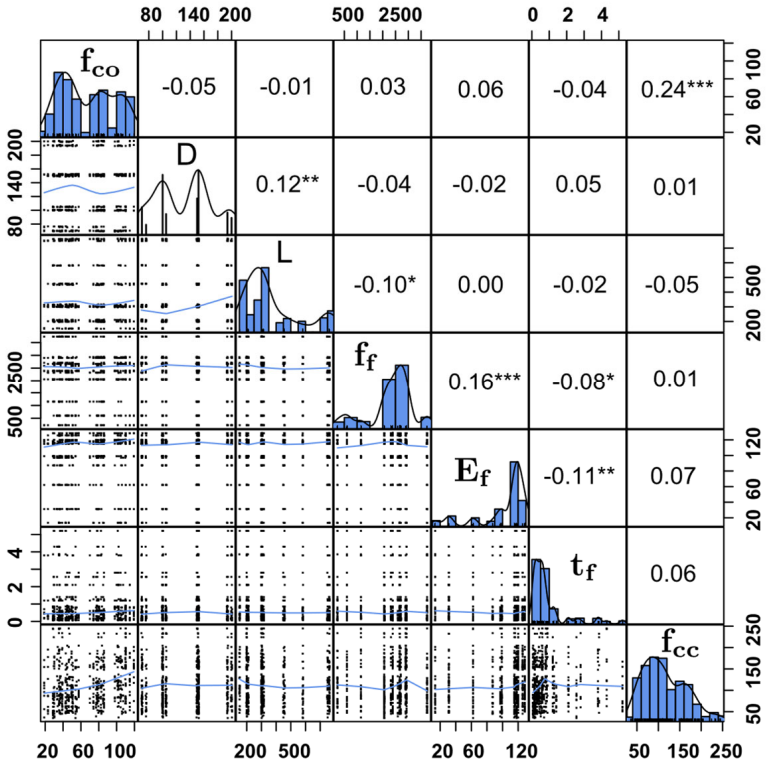

Figure 1. Correlation plot of the features.

The statistical properties of the input and output variables are listed in Table 3. A visual representation of the input and output feature ranges in the database are displayed in Figure 2. Each feature was separated into four subranges, such that the lower and upper bounds of a subrange correspond to a quarter of the entire range of a feature. Furthermore, the size of each subgroup in the horizontal direction is in proportion to the number of data samples belonging to that subgroup. The number of data points in every subgroup is written inside the horizontal bar of that subgroup. The lower and upper bounds of the groups are written above their boundaries. According to Figure 2, the unconfined (f_{co}) and confined (f_{cc}) compressive strength values of concrete were relatively evenly distributed. On the other hand, in the case of the AFRP wrap thickness (t_f), the thickness value was less than 1.4 mm in 84% of the entire dataset. Also, in the case of the AFRP elasticity modulus (E_f), 82% of the data samples had an elasticity modulus greater than 71.1 GPa. The lengths of the specimens were less than 457 mm in 75% of the samples and less than 610 mm in 85% of the samples. Due to missing data, the enhanced dataset for the prediction of the ultimate confined concrete strain (ε_{cu}) consisted of 477 samples, whereas the models for the prediction of f_{cc} were trained on a dataset consisting of 675 samples. In both datasets, the number of synthetically generated data points was twice as big as the number of real data points.

Table 3. Statistical properties of the input and output variables.

Variable	Min.	Max.	Mean	Standard Dev.	Skewness	Kurtosis
f_{co} [MPa]	18.9	119.3	67.55	29.24	0.191	−1.344
d [mm]	70	200	130.9	40.07	0.118	−1.062
L [mm]	152	762	368.3	190.3	1.124	−0.055
f_f [MPa]	230	3732	2318	859.8	−0.934	0.513
E_f [GPa]	13.6	128.5	101.5	32.35	−1.575	1.222
t_f [mm]	0.057	5.21	0.919	1.115	2.252	4.613
f_{cc} [MPa]	35.16	244.6	114.3	49.20	0.601	−0.373
ε_{cu} [%]	0.24	4.78	1.924	1.016	0.328	−0.645

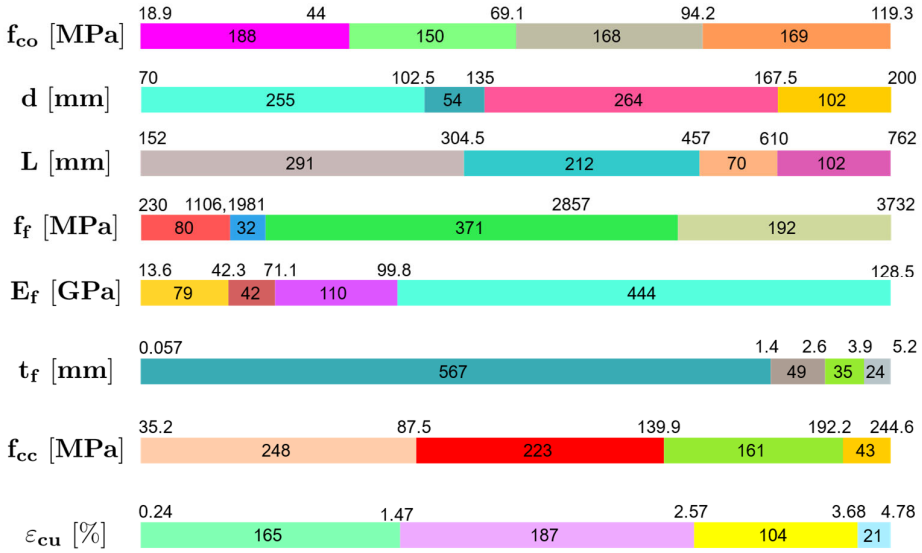

Figure 2. Feature ranges.

2.3. Machine Learning Methodologies

A brief theoretical overview of the machine learning models used to predict the compressive strength and ultimate tensile strain of AFRP-confined concrete is given in this section. A novel approach was proposed for generating large datasets, using tabular generative adversarial networks (TGAN), which is explained in Section 2.3.2. In order to quantify the impacts of different input features on the machine learning model output, the SHapley Additive exPlanations (SHAP) approach was employed. The SHAP algorithm is introduced in Section 2.3.3. A flowchart of the entire machine learning model generation process is given in Figure 3.

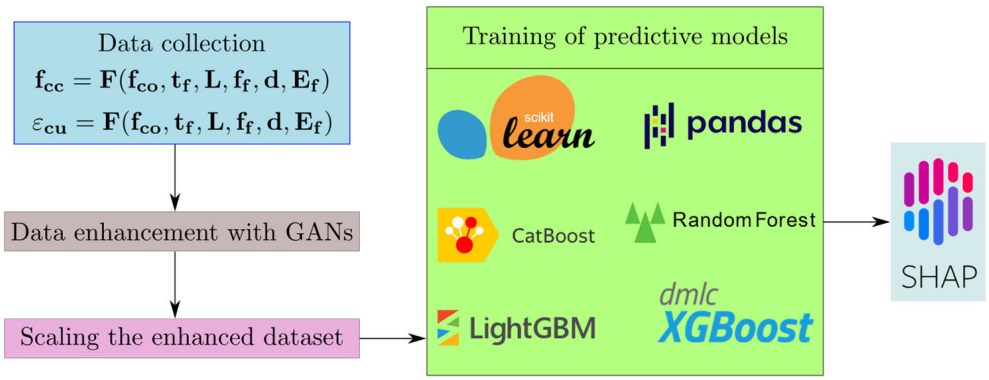

Figure 3. Machine learning flowchart.

2.3.1. Gradient Boosting Methods

Gradient boosting algorithms, such as XGBoost, CatBoost, LightGBM and extra trees regressor, are based on the combination of individual decision tree predictions to generate a strong learning algorithm. The algorithms produce a sequence of decision trees, with the goal of every new decision tree being a correction for the prediction errors made by the preceding decision trees. The combination of decision tree predictions to generate a strong learner is described in Equation (2), where **x** is a data point, N is the predictive model's total number of decision trees, $f_i(\mathbf{x})$ is the prediction of an individual decision tree with index i and $f(\mathbf{x}) = \hat{y}$ is the model output:

$$\hat{y} = f(\mathbf{x}) = \sum_{i=1}^{N} f_i(\mathbf{x}) \tag{2}$$

$$L = \sum_{k=1}^{n} d(\hat{y}_k, y_k) \tag{3}$$

During each tree iteration, the gradient boosting method aims to minimize the loss function L, given in Equation (3), where d is a function measuring the distance between the target value y_k and the prediction $\hat{y}_k$ and n is the total number of data points in the training set.

2.3.2. Tabular Generative Adversarial Networks (TGAN)

The availability of large and high-quality datasets is necessary for the use of machine learning techniques in the area of engineering systems modeling. However, the generation of statistically significant amounts of data points using traditional experimental methods can be a costly process. Generative adversarial networks (GANs) have been proposed recently as an alternative approach for generating large synthetic datasets on which state-of-the-art ML models can be trained [50,51]. GANs consist of two components called the generative model and the discriminator model. These two components are trained at the same time, whereby the generative model constantly generates data samples which increasingly resemble the data points from the real dataset, and the discriminator model classifies the newly generated points as real or synthetic. The aim of this training process is to bring the generative model to the point where the newly generated data points are indistinguishable by the discriminator model from real data [52]. In this study, the synthetic dataset was generated using the CTGAN software library for the Python programming language [53]. The synthetic data points were generated in such a way that the features had a similar probability distribution to the original data and the same upper and lower bounds. The process of generative model training is described in Equation (4).

$$\min_G \max_D V(D,G) = E_{x \sim p_{data}(\boldsymbol{x})}[\log D(\boldsymbol{x})] + E_{z \sim p_z(z)}[\log(1 - D(G(z)))] \tag{4}$$

In Equation (4), $x, p_{data}(x), z, p_z(z), D(x)$, and $G(x)$ denote a data point, the probability distribution of the real dataset, a random noise vector, the prior probability distribution of z, the discriminator model and the generator model, respectively. Equation (4) describes a mini-max game between the generator ($\boldsymbol{G}$) and the discriminator ($\boldsymbol{D}$) with the value function $\boldsymbol{V}(\boldsymbol{D}, \boldsymbol{G})$ [52].

2.3.3. SHapley Additive exPlanations (SHAP)

SHapley Additive exPlanations (SHAP) summary plots are visual depictions of the influence each input variable has on the predicted quantity. In recent years, the SHAP approach has been frequently applied in order to explain ML models [54–59]. In SHAP summary plots, each data sample is represented by a dot, the color of which is determined by the feature value. The horizontal position of each dot in the SHAP summary plots gives information about the impact of the input feature on the model output, such that features

with an increasing impact on the model output are placed on the right-hand side of the summary plot, and those with a decreasing impact are placed on the left-hand side. The farther a dot is positioned to the right- or left-hand side of the zero point, the greater impact this feature has on the model output. The dots colored in the shades of red indicate the high value of an input feature whereas dots colored in the shades of blue indicate the low value of an input feature. The changes in the prediction when a feature is removed from the model provide the basis for the SHAP values ϕ_i, which control a sample's location along a horizontal direction. The computation formulas of these values are expressed in Equations (5) and (6):

$$g(x^{'}) = \phi_0 + \sum_{i=1}^{M} \phi_i x' \tag{5}$$

$$\phi_i = \sum_{S \subseteq F\{i\}} \frac{|S|!(|F| - |S| - 1)!}{|F|!} \left[f_{S \cup \{i\}} \left(x_{S \cup \{i\}} \right) - f_S(x_S) \right] \tag{6}$$

In Equation (5), M is the total number of input features and g is an explanation function, which linearly combines the simplified input features x', which only take values from the set {0, 1}. The Shapley values, ϕ_i, are the coefficients of this linear combination. These simplified input features are related to the actual input values by a mapping function, h, with $x = h(x')$. The computation of ϕ_i values is shown in Equation (6), where F denotes the set of all input features, S denotes a subset of F which does not include the input feature with index I, and f represents the predictive model. Further explanations of the SHAP methodology can be found in [60].

3. Results

This section presents the results of various machine learning techniques in predicting the ultimate strain capacity and the compressive strength of AFRP-confined concrete. The performances of the ML models have been compared to some of the predictive equations available in the literature.

3.1. Performances of the Predictive Equations

The equations investigated in this section are listed in Tables 1 and 2. For each one of these equations, the predicted f_{cc} and ε_{cu} values are plotted against the actual experimental measurements. The coefficient of determination (R^2), mean absolute error (MAE), and root mean squared error (RMSE) metrics are utilized in order to quantify the accuracies of these predictions. The deviations of the predicted values from the measurements are shown with dotted lines in Figures 4 and 5. The relationships between the equation predictions are also visualized using Taylor diagrams and the Pearson correlation coefficient.

The performances of the equations in predicting the confined ultimate strength of concrete are listed in Table 4. According to the error metrics in Table 4, the equations were far from accurate. In particular, the negative values of the R^2 score are an indicator of low prediction accuracy. Also, the plotted predictions in Figure 4 show that the predicted values can be more than 120% lower or more than 60% greater than the actual values. The equations proposed by Wu et al. [21], Wang and Wu [22] and Lobo et al. [24] tend to overestimate the ultimate strength and, for some of the specimens, this overestimation is nearly 60%. On the other hand, the equations proposed by Djafar-Henni and Kassoul [23] tend to underestimate the ultimate strength, and this underestimation can exceed 120% for some of the data samples. A similarly low accuracy of prediction was also observed in the equations for the prediction of the ultimate strain. Figure 5 displays the plot of the experimental ultimate strain values against the predicted values. The equations developed by both Wu et al. [21] and Lobo et al. [24] tend to underestimate the ultimate strain, although, for some of the data samples, these equations can also overestimate the ultimate strain by more than 60%. The accuracy of these two models have been determined by error metrics and listed in Table 5. Again, the negative values of the R^2 scores in Table 5 indicate the poor performance of these predictive equations.

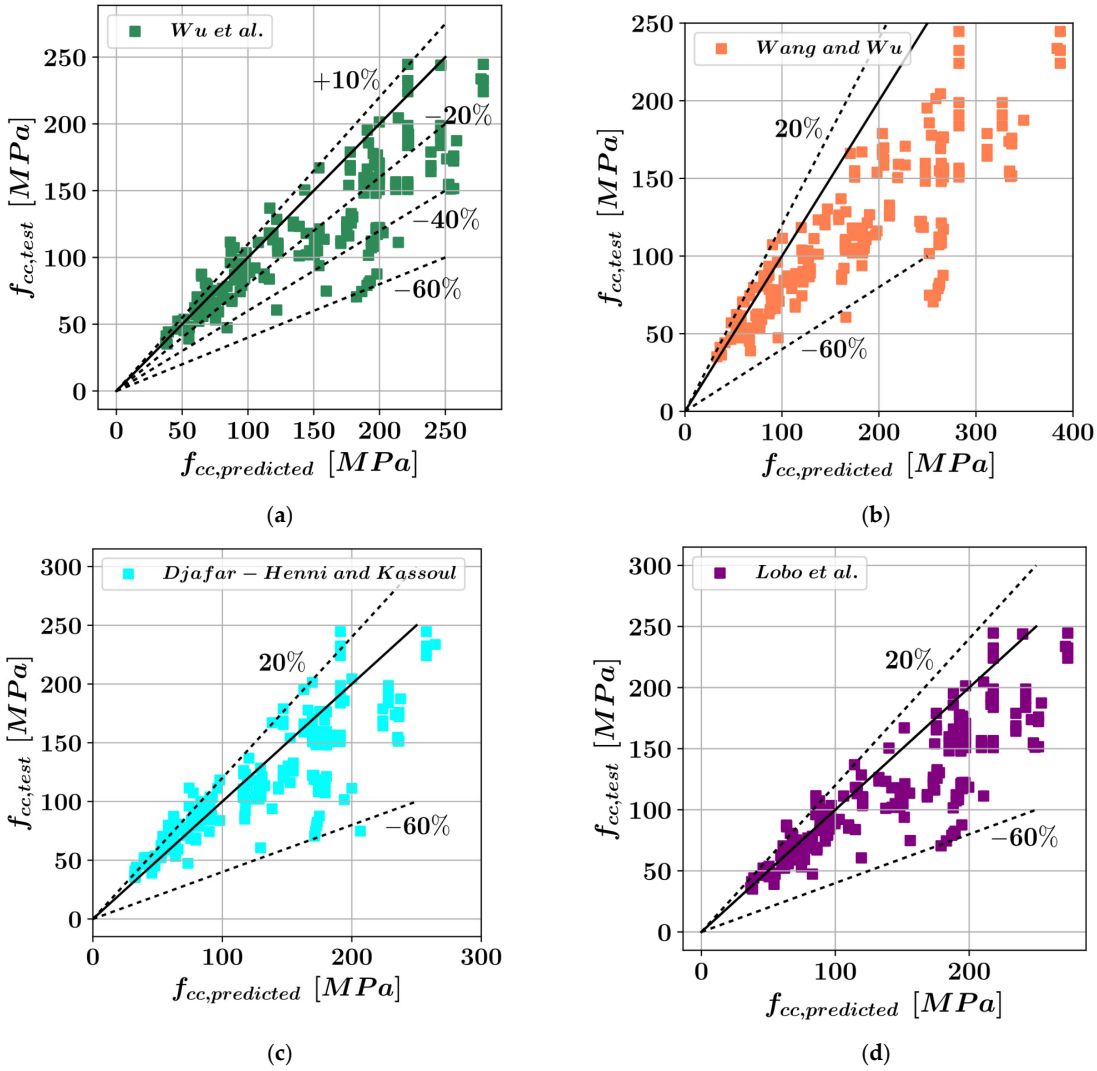

Figure 4. Equation predictions for the confined compressive strength, according to (**a**) Wu et al. [21], (**b**) Wang and Wu [22], (**c**) Djafar-Henni and Kassoul [23] and (**d**) Lobo et al. [24].

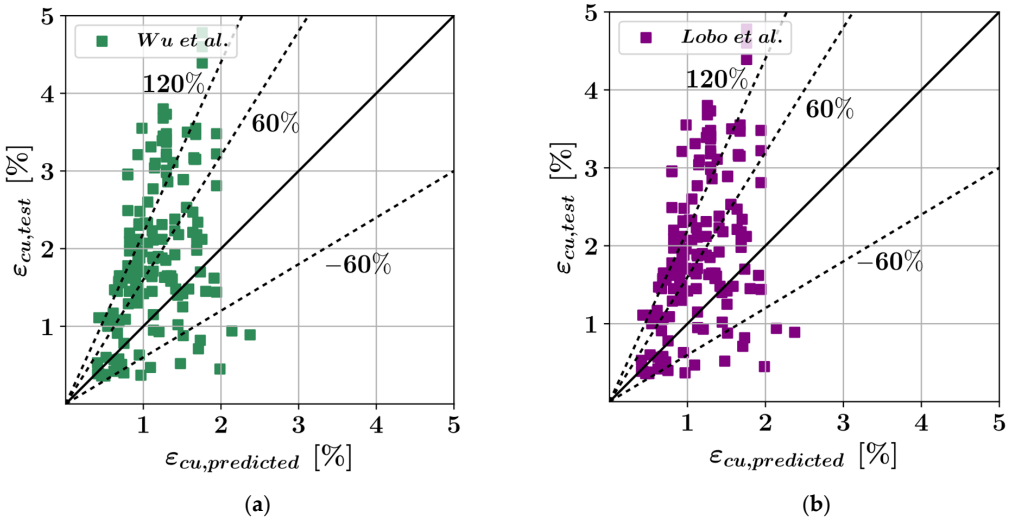

Figure 5. Equation predictions for the confined compressive strength, according to (**a**) Wu et al. [21] and (**b**) Lobo et al. [24].

Table 4. Equation performances for compressive strength prediction.

Equation	R^2	MAE [MPa]	RMSE [MPa]
Wu et al. [21]	0.7610	31.34	43.17
Wang and Wu [22]	0.6592	72.44	104.8
Djafar-Henni and Kassoul [23]	0.6527	41.79	51.48
Lobo et al. [24]	0.7647	29.56	41.05

Table 5. Equation performances for ultimate strain prediction.

Equation	R^2	MAE [%]	RMSE [%]
Wu et al. [21]	0.1869	0.9622	1.186
Lobo et al. [24]	0.0030	1.638	1.909

3.2. Performances of the ML Models

The confined compressive strength values predicted by the ML models are plotted against the experimental measurements in Figure 6. The predictions on the training set and the test set are plotted in different colors in each plot. Also, the ±10% deviation lines from a perfect match between the actual and predicted values are shown on each plot. The performances of these ML models have been quantified using the same four error metrics used to determine the accuracy of the equations in Tables 4 and 5. Among these four metrics, a R^2 score value close to one indicates high prediction accuracy. In addition to their accuracy of prediction, the ML models have also been investigated with respect to their computational speed. According to the listed values in Table 6, the extra trees model performed best on the test set, in terms of all error metrics. In terms of computational speed, the support vector regressor (SVR) model was the fastest, although this model performed significantly worse than the remaining models in terms of prediction accuracy. Among the five ensemble learning models listed in Table 6, LightGBM was the worst-performing model in terms of all error metrics.

Figure 7 shows the first of the 100 decision trees constituting the XGBoost model developed for the prediction of f_{cc}. In Figure 7, the root node tests the value of the unconfined ultimate strength (f_{co}). It should be mentioned that the values in Figure 7 are scaled values, except for the values in the leaf nodes. If the condition inside the root node or an internal node is true, or the feature value is missing in a particular data sample, then the node branches towards the left-hand side; otherwise, it branches towards the right-hand side. The tree consists of 27 internal nodes, splitting at different levels of AFRP jacket thickness (t_f), unconfined ultimate strength (f_{co}), elasticity modulus of the AFRP wrap (E_f), specimen diameter (D), specimen length (L) and AFRP ultimate tensile strength (f_f). There are 29 green colored leaf nodes, one of which is selected as the tree output, depending on the outputs of the previous internal nodes and the root node. By adding up all of the decision tree outputs, the XGBoost model's output is determined.

Table 6. Model performances on compressive strength prediction.

Algorithm	R^2		MAE [MPa]		RMSE [MPa]		Duration [s]
	Train	Test	Train	Test	Train	Test	
XGBoost	0.9792	0.9371	2.530	6.135	7.080	12.16	5.24
CatBoost	0.9232	0.9064	9.965	10.01	13.61	14.84	12.62
Random Forest	0.8729	0.9228	13.17	8.343	17.52	13.47	6.47
LightGBM	0.7894	0.8837	17.10	11.65	22.55	16.54	9.59
Extra trees	0.9799	0.9383	1.812	5.438	6.958	12.05	7.26
KNN	0.9510	0.9090	3.091	6.182	10.35	14.63	4.70
SVR	0.2849	0.3063	30.74	34.70	40.29	43.16	0.01

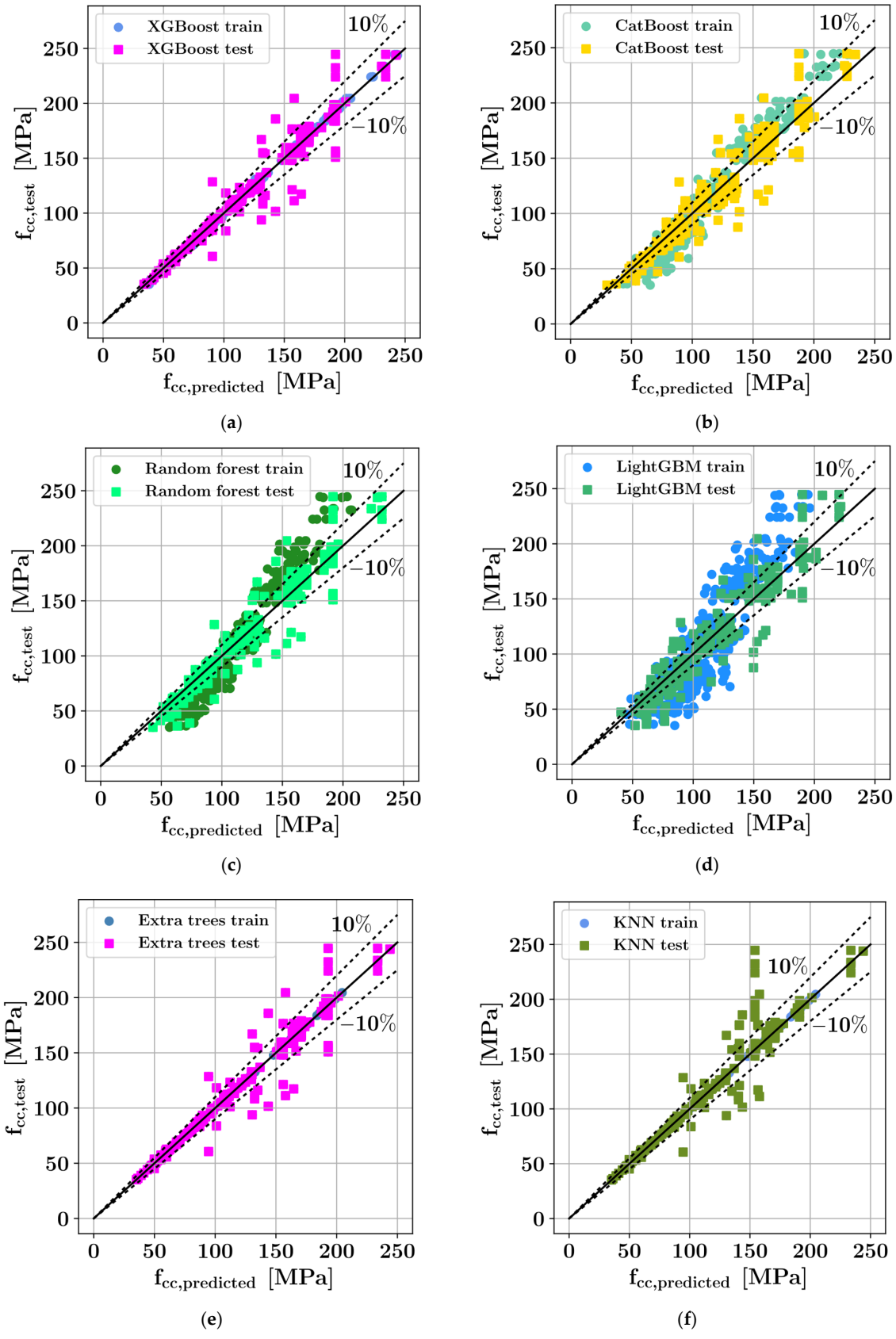

Figure 6. ML predictions of the compressive strength using (**a**) XGBoost, (**b**) CatBoost, (**c**) Random Forest, (**d**) LightGBM, (**e**) Extra Trees, and (**f**) KNN.

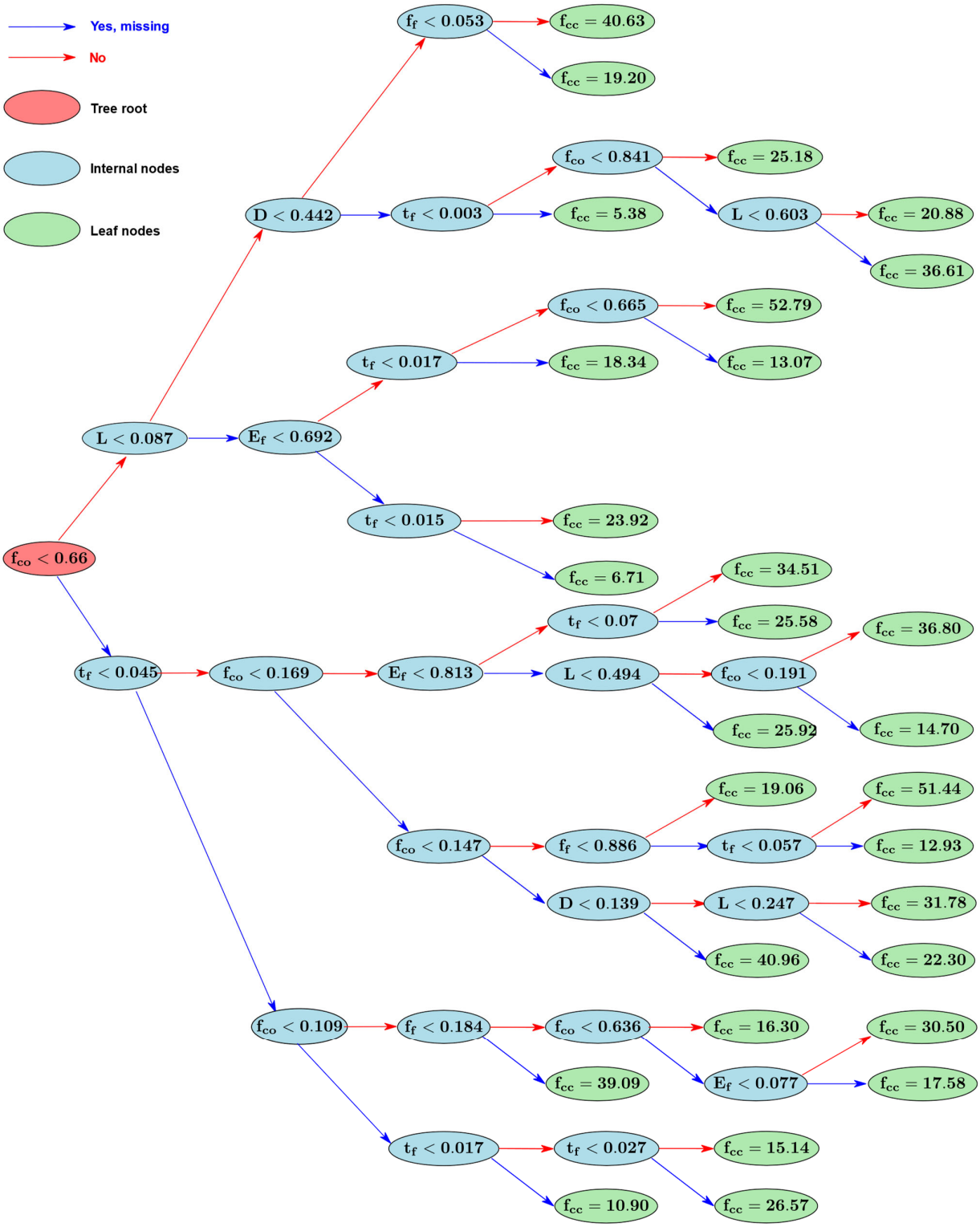

Figure 7. First tree of the XGBoost model for the prediction of f_{cc}.

Figure 8 and Table 7 present the performances of the ML models in predicting the ultimate strain of AFRP-confined concrete specimens. Due to the data availability limitations, a reduced dataset, consisting of 159 samples, was used in the generation of the synthetic dataset. This dataset reduction was caused by missing values for the unconfined concrete ultimate strain. For the training and testing of the ML models, a dataset consisting of 477 samples was used, which consisted of both synthetic and real data points. Clearly,

the predictions for most of the specimens in the database with 477 samples lie within 10% distance from the target values. Also, Table 7 shows that the R^2 score for all of the ML models was greater than 0.7 on the test set. Furthermore, excluding the SVR algorithm, minimum R^2 scores of 0.8837 and 0.8155 can be observed for compressive strength and ultimate strain, respectively. In terms of the mean absolute error metric, the most accurate predictions on the test set were made by the extra trees regressor, followed by the K-nearest-neighbors (KNN) algorithm. In terms of R^2 score, the XGBoost model was the second-best-performing model in the prediction of the ultimate strain.

The performances of the different ML models and the equations are also presented, with Taylor diagrams for both ultimate strength and ultimate strain cases, in Figure 9, where each set of predictions is represented with a dot of different color. In Figure 9, the standard deviations of each set of predictions are shown on the horizontal and vertical axes. The standard deviation value, corresponding to a particular prediction set, can be found with the help of circular arcs. In each Taylor diagram, the original dataset is represented with a blank dot. The Pearson correlation values for each prediction set are shown on the radial axis.

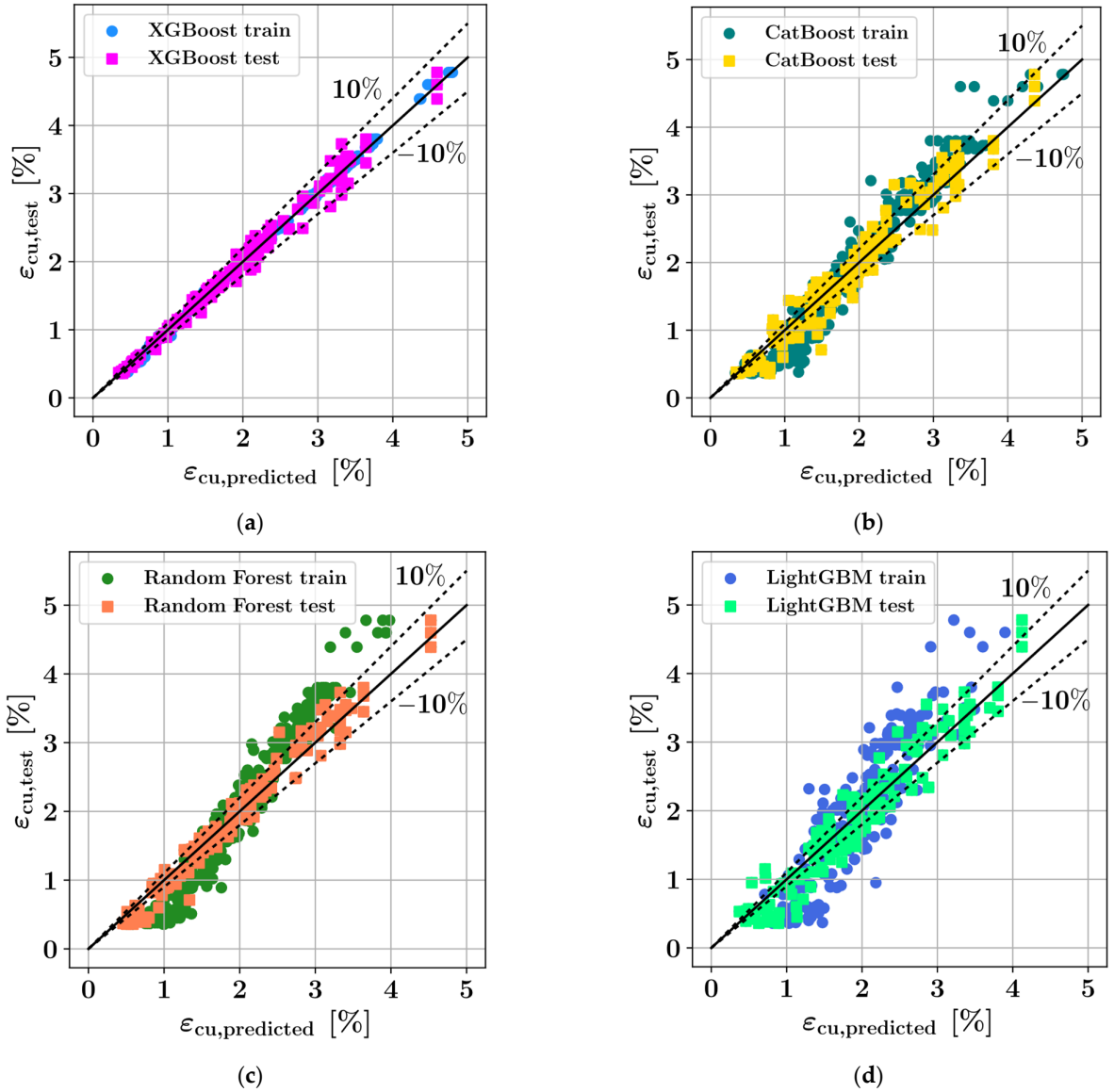

Figure 8. *Cont.*

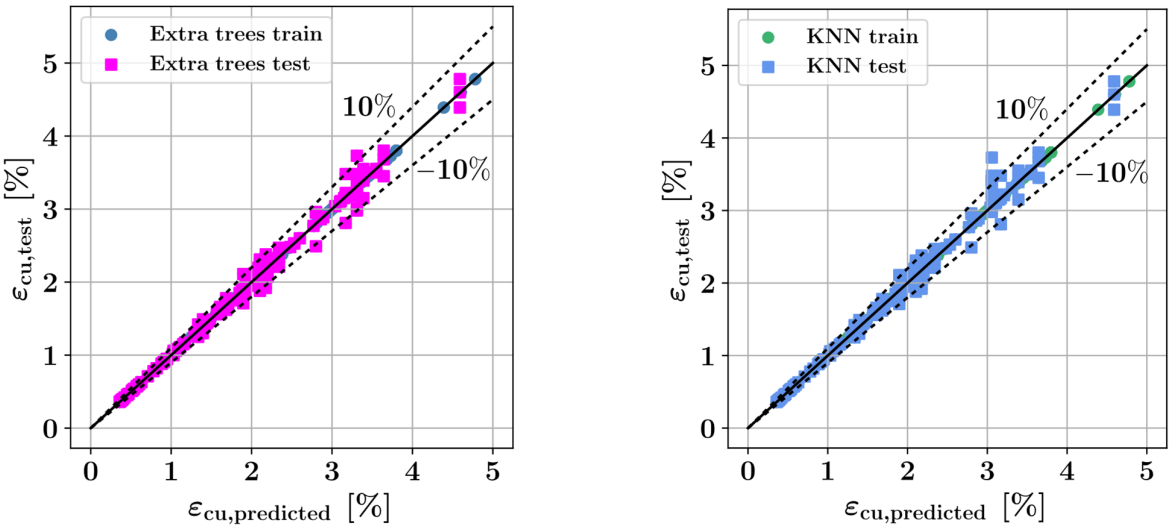

(**e**) (**f**)

Figure 8. ML predictions for the ultimate strain using (**a**) XGBoost, (**b**) CatBoost, (**c**) Random Forest, (**d**) LightGBM, (**e**) Extra Trees, and (**f**) KNN.

Table 7. Model performances in the ultimate strain prediction.

Algorithm	R^2		MAE [%]		RMSE [%]		Duration [s]
	Train	Test	Train	Test	Train	Test	
XGBoost	0.9966	0.9879	0.0303	0.0708	0.0579	0.1076	5.64
CatBoost	0.9508	0.9385	0.1677	0.1857	0.2169	0.2471	15.37
Random Forest	0.9694	0.8863	0.1306	0.2606	0.1711	0.3362	7.93
LightGBM	0.9242	0.8155	0.2228	0.3378	0.2693	0.4278	11.59
Extra trees	0.9962	0.9899	0.0117	0.0485	0.0480	0.0979	5.16
KNN	0.9968	0.9862	0.0129	0.0537	0.0564	0.1148	4.28
SVR	0.8547	0.7084	0.2628	0.4445	0.3640	0.5665	3.17

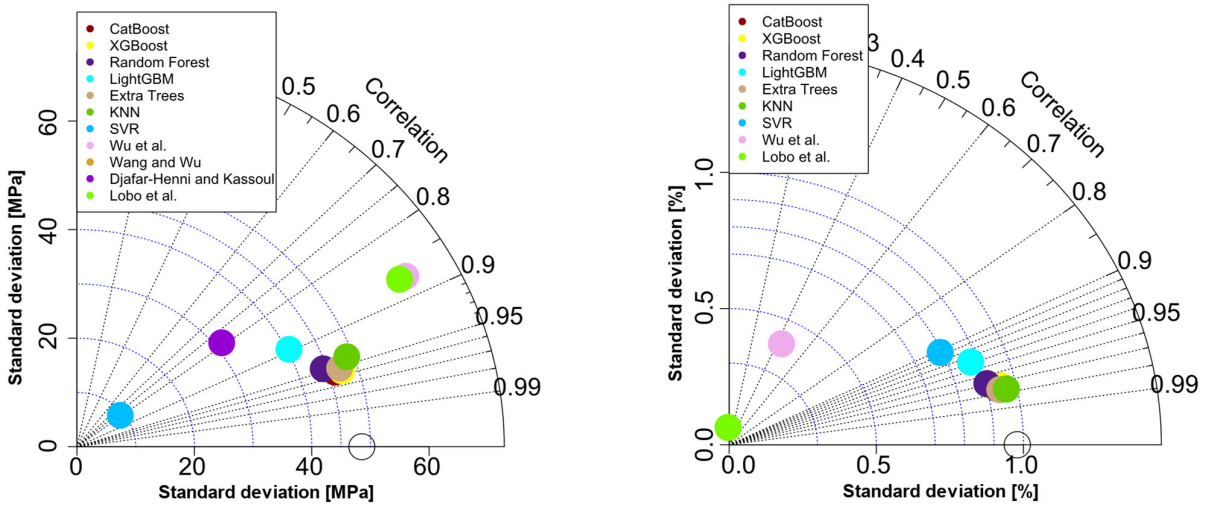

(**a**) (**b**)

Figure 9. Taylor diagrams for the prediction of (**a**) ultimate strength and (**b**) ultimate strain.

3.3. SHAP Interpretation of the ML Models

The SHAP summary plot presented in Figure 10 indicates that the predicted value of the confined concrete ultimate strength is most significantly influenced by the unconfined concrete ultimate strength, followed by the total thickness of the AFRP jacket and the length of the specimen. On the other hand, the elasticity modulus of the AFRP has the least impact on the model output. Since the dots representing f_{co} have red colors to the right-hand side of the diagram, increasing the value of f_{co} also increases the impact of f_{co}. A similar relationship also exists between t_f and f_{cc}. However, the opposite is true for the length and diameter of the specimen, such that increasing these two quantities has a decreasing effect on the predicted f_{cc} values.

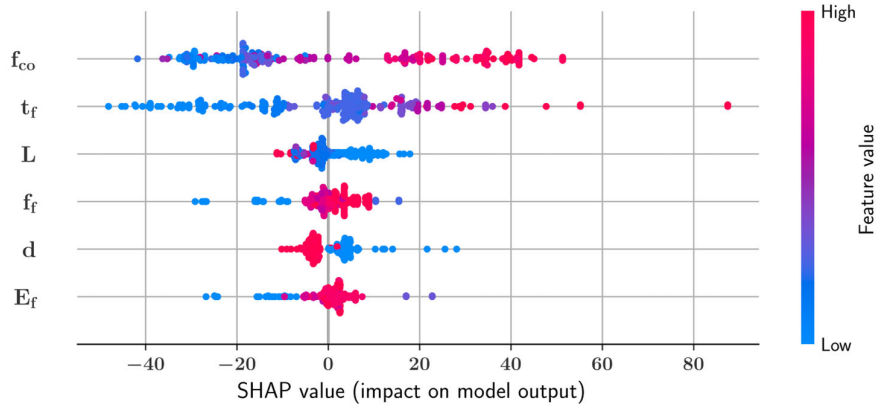

Figure 10. SHAP summary plot of the CatBoost model for f_{cc} prediction.

The feature dependence plots in Figure 11 further elaborate on the change in the model predictions, with regard to the four factors that have the largest effect, as demonstrated by the SHAP summary plot. Each feature dependence plot in Figure 11 contains information about two input features. The feature represented with the color bar to the right-hand side of the plot is the input feature most dependent on the feature represented on the horizontal axis. The values of the dependent feature affect the colors of the dots in Figure 11, and each one of these dots represents one of the samples from the dataset. Figure 11a illustrates how the SHAP value of f_{co} rises in tandem with the value of f_{co}. For values of f_{co} less than 80 MPa, the addition of f_{co} into the model has a decreasing effect on the model output, whereas, for values of f_{co} greater than 80 MPa, the addition of f_{co} increases the model predictions. Similar trends can also be observed for E_f and f_f, whereas the opposite trend can be observed for the specimen length L. For values of L less than 300 mm, the addition of this parameter into the model increases the predictions, whereas, for L values greater than 300 mm, the length of the specimen has a decreasing effect on the model outputs.

A SHAP summary plot is shown in Figure 12 for the CatBoost model, which predicts the confined ultimate strain. The ultimate tensile strength of AFRP (f_f) was found to have the greatest impact on the model predictions, followed by the unconfined ultimate strength and the AFRP jacket thickness. It was observed that the specimens' diameter had the least influence on the model predictions. Figure 13 shows the feature dependence plots for the four parameters with the greatest impact, according to Figure 12. According to Figure 13a, the increase in the value of f_f also increases the SHAP value of this feature. Particularly at values greater than 2500 MPa, f_f has an increasing effect on the model output. A similar trend can also be observed between t_f and its impact on the model output in Figure 13d. Up to a thickness of 0.3 mm, the confining jacket thickness has a decreasing effect on the predictions, whereas, at greater thickness values, the addition of the jacket thickness increases the model predictions. The effect of the specimen length on the predicted ε_{cu} values is similar to the case of the f_{cc} prediction, such that, at higher levels of specimen length, the addition of this variable into the models decreases the predicted ε_{cu} values. Figure 13b shows that, up to 80 MPa, an increase in f_{co} leads to lower SHAP values of

this variable, which indicates a decreasing effect on the ultimate strain predictions. For f_{co} values greater than 80 MPa, the SHAP values of f_{co} are spread in a wider range.

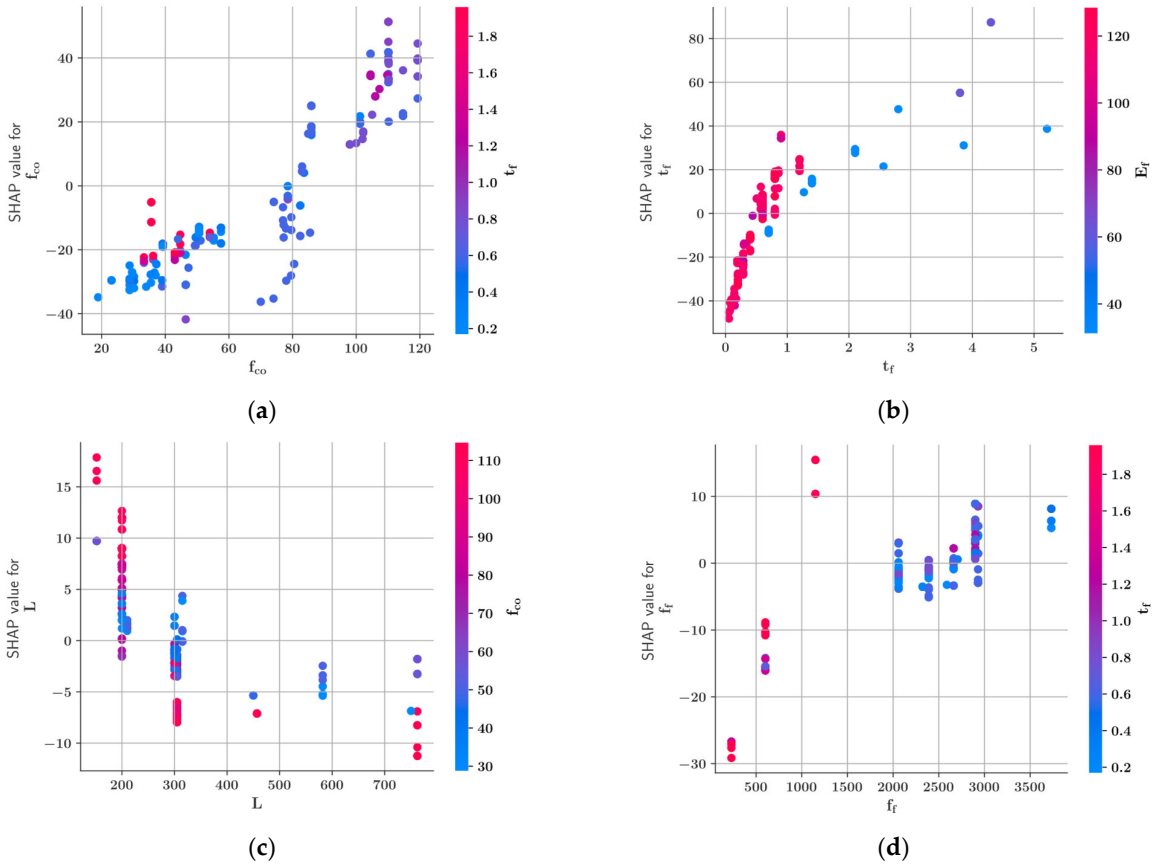

Figure 11. CatBoost ultimate strength prediction feature dependence plots for (**a**) f_{co} (**b**) t_f, (**c**) L and (**d**) f_f.

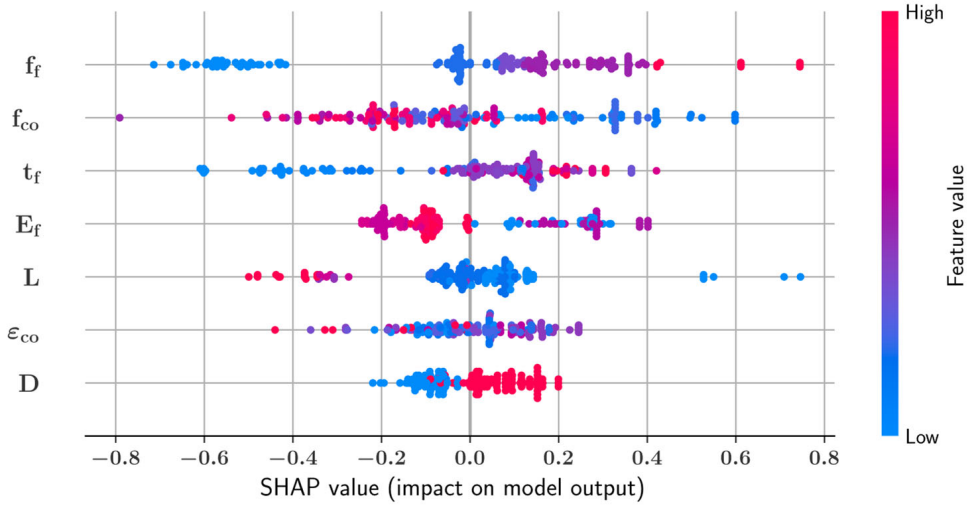

Figure 12. SHAP summary plot of the CatBoost model for ε_{cu} prediction.

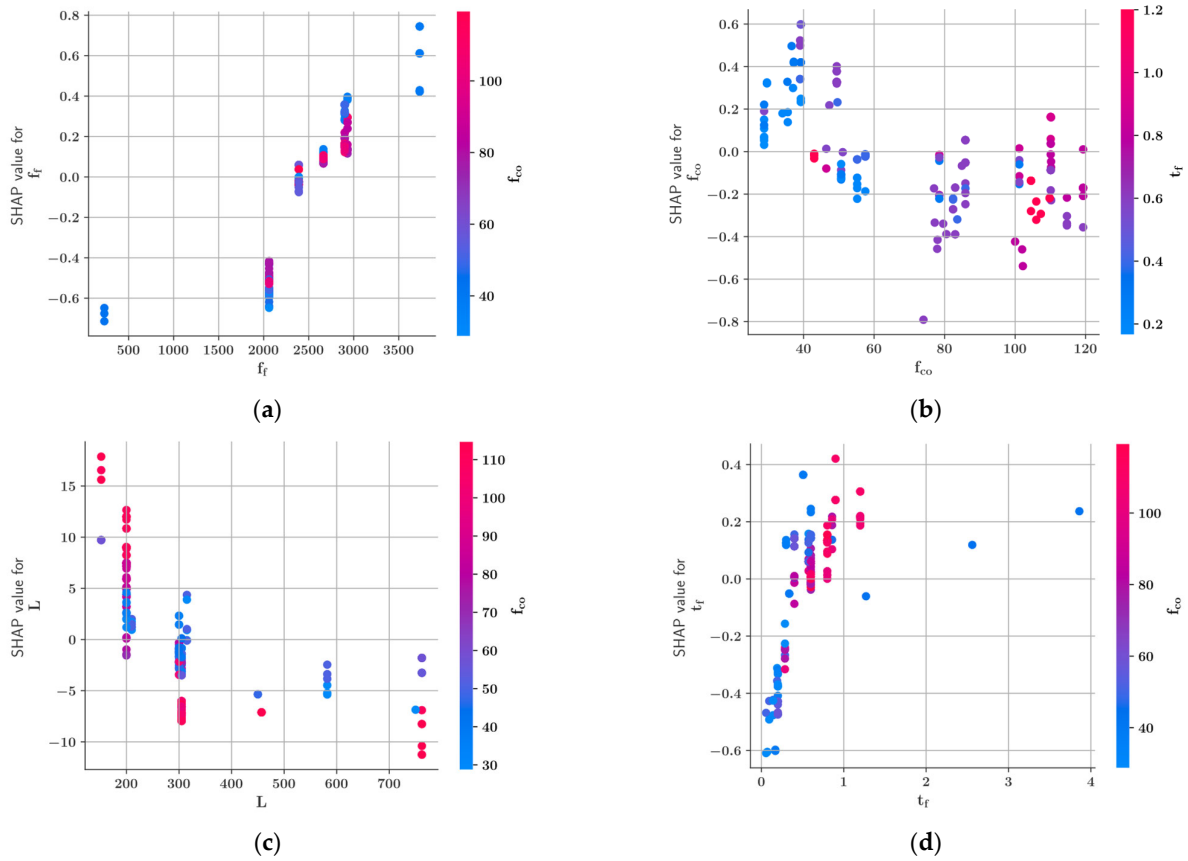

Figure 13. CatBoost ultimate strain prediction feature dependence plots for (**a**) f_f, (**b**) f_{co}, (**c**) L and (**d**) t_f.

3.4. Individual Conditional Expectation (ICE) Interpretation of the ML Models

The ICE plots in Figures 14 and 15 show how the model predictions vary in relation to a certain input feature while all other features have fixed values. The input features for the generation of the ICE plots have been selected based on their impacts on the model outputs. The ICE curves are generated for each data sample separately, which clarifies the differences between the data samples, in terms of their interaction with the predictive model. In each ICE plot, the average of all curves is represented with a thick blue line. In the ICE plots, all of the curves being close to one another indicates a similar variation of the predicted quantity in all samples. Curves that lie farther away from the average indicate a larger deviation of the predictions from the average. For instance, in the ICE plots of Figures 14a and 15b, all of the generated curves lie relatively close to the average curve, whereas, in Figures 14c and 15a, the curves are further apart from each other, indicating a larger variation of the predictions. According to Figure 14a, the confined ultimate strength f_{cc}, which is denoted with f(x) in Figure 14, continuously increases with f_{co}. The largest increase in f_{cc} occurs in the interval 75 MPa $\leq f_{co} \leq$ 100 MPa. A similar trend is also observed in $f(x)|t_f$, and the largest increase happens for $t_f \leq 2$ mm. Figure 15 shows the variation of the predicted ε_{cu} denoted with f(x). The adverse effect of increasing the column length on the ultimate strain can be seen in Figure 14c. Although f_{co} has, overall, an increasing effect on the ultimate strength according to Figure 13a, a different trend can be observed in Figure 15b, where increasing the value of f_{co} in the range 20 MPa $\leq f_{co} \leq$ 80 MPa is shown to have a decreasing effect on the ultimate strain.

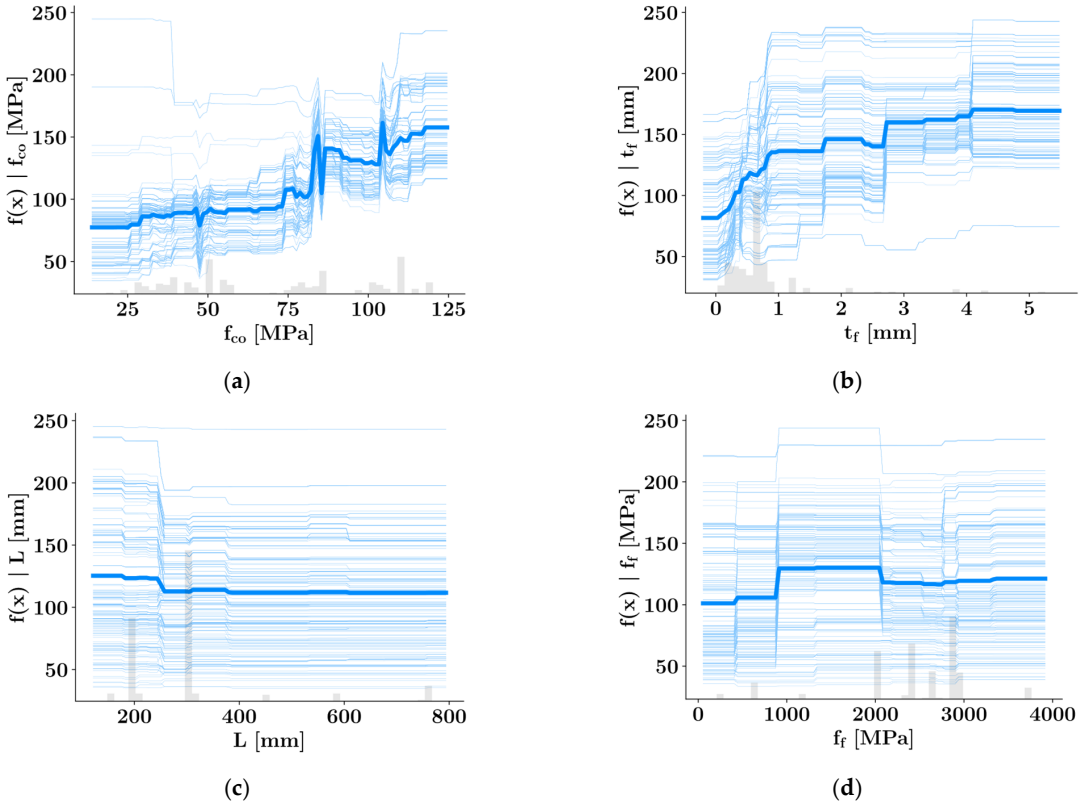

Figure 14. ICE plots of the XGBoost ultimate strength prediction for (**a**) f_{co}, (**b**) t_f, (**c**) L and (**d**) f_f.

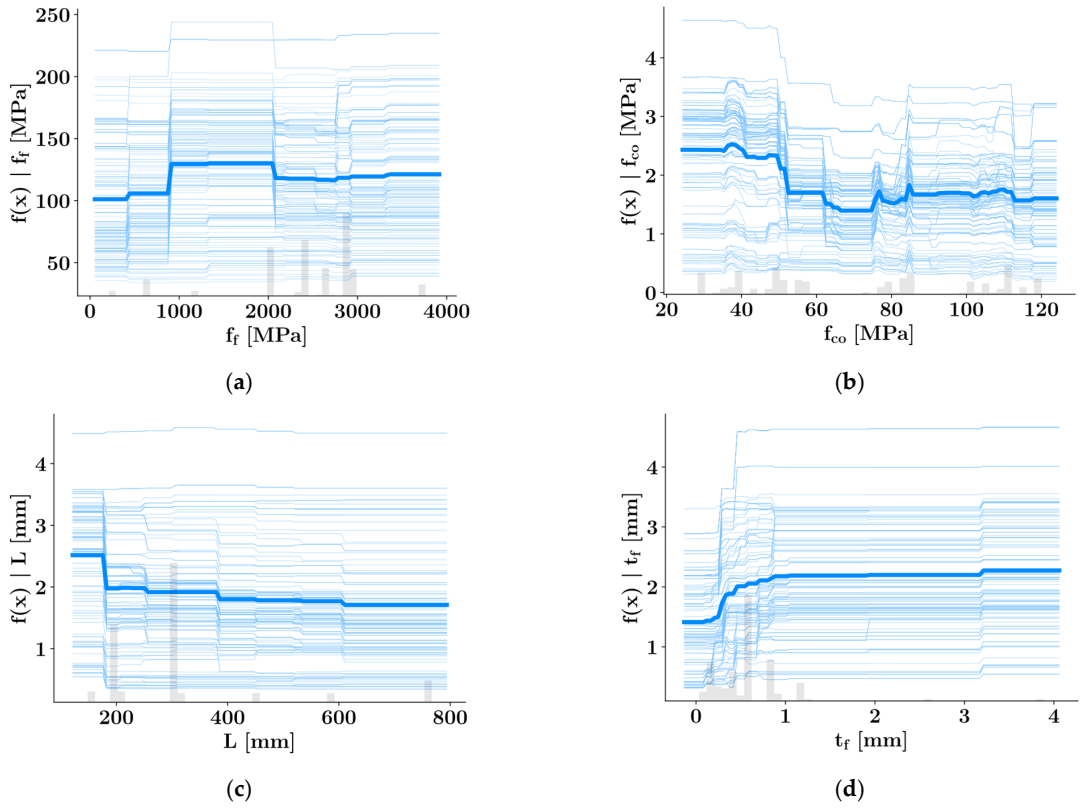

Figure 15. ICE plots of the XGBoost ultimate strain prediction for (**a**) f_f, (**b**) f_{co}, (**c**) L and (**d**) t_f.

4. Discussion

FRP materials are finding increasing numbers of applications in many areas of engineering in recent years. Particularly in structural retrofitting, the application of FRP jackets is a widely used alternative to steel confinement. As an alternative to carbon and glass fibers, aramid fibers are also finding applications in this area, due to their favorable ductility and strength properties. However, the lack of reliable equations can be a significant hurdle in the way of wide-scale applications of these materials in engineering design.

The current study showed the application of state-of-the-art ensemble learning techniques in mechanical properties predictions of AFRP-confined concrete. A dataset gathered from the literature served as the basis for training the machine learning models. The reliability and accuracy of machine learning models can be increased in proportion to the size of their training dataset. Based on this assumption, the current study proposes a novel technique of generating additional data points using generative adversarial networks (GANs). These models consist of a generator and a discriminator component, where the performance of the generator component iteratively improves, such that the newly generated data points are indistinguishable from the original data points. It was shown that the predictive models trained on the dataset enhanced with the synthetic data points can significantly outperform the predictive equations currently available in the literature. One of the major reasons for the inaccuracy of the equations is that most of the equations in the literature are developed based on regression techniques fine-tuned towards a particular dataset and therefore cannot be generalized sufficiently. Therefore, it is crucial to train any statistical model on a large enough dataset.

In the next stage of the study, the machine learning models have been further investigated using the SHapley Additive exPlanations (SHAP) approach. The SHAP results provide explanations for the predictive models by measuring the contribution of different input features to the model output. Using the SHAP technique, the input features have been ranked with respect to their impact on the model predictions for the confined compressive strength and ultimate strain. The unconfined compressive strength of concrete and the ultimate tensile strength of the AFRP wrap have been found to be the most impactful input features in the prediction of the confined compressive strength and ultimate tensile strain, respectively. Finally, the variations of the confined compressive strength and ultimate strain, with respect to different input features, have been visualized using individual conditional expectations plots.

5. Conclusions

This study demonstrated the usage of modern ensemble learning and data enhancement techniques for data-driven predictions of the structural capacity of columns confined by AFRP material. The datasets have been enhanced using synthetic data points created by generative adversarial networks (GANs). The major points of this paper can be summarized as follows:

- To predict the ultimate strength and strain of AFRP-wrapped concrete columns, seven different predictive models were developed on datasets of 225 and 159 data points, respectively. The sizes of these datasets have been further increased using data points synthetically generated by generative adversarial networks.
- The machine learning techniques performed significantly better than the predictive equations adopted from the literature. Particularly, the extra trees, XGBoost, and KNN models were the best performing models in the prediction of the ultimate strength and ultimate strain.
- The unconfined ultimate strength of concrete and the elasticity modulus of AFRP were found to have the greatest and least impact on the predicted f_{cc} values, respectively. Plots of individual conditional expectations (ICE) and feature dependency were used to illustrate the increasing impact of unconfined ultimate strength on confined ultimate strength. In certain ranges the unconfined ultimate strength was shown to have a decreasing effect on the ultimate strain of the specimens.

- The ultimate tensile strength of AFRP and the column diameter were found to have the greatest and least impact on the predicted ε_{cu} values, respectively.
- The variations of the predicted ultimate strength and ultimate strain values, with respect to the most impactful input features, were visualized using ICE plots.
- It was shown that the equations in the literature can significantly overestimate the compressive strength and ultimate strain of confined concrete.

This study presented the possibility of increasing the dataset sizes used in predictive model training. Although promising results could be obtained through these ML techniques, the proposed methodology is not recommended to be adopted in practical applications until further validation is undertaken on significantly larger experimental datasets. In particular, in the development of predictive models for the ultimate strain, a reduced dataset has been employed as a base model for the GAN due to the missing values for the ultimate strain values. Future studies in this field should be carried out with larger datasets for both ultimate strength and ultimate strain predictions. Also, predictive models for rectangular columns can be developed in future studies.

Supplementary Materials: The following supporting information can be downloaded at GitHub link: https://github.com/ccakiroglu/AFRP (accessed on 27 October 2023). A dataset of 225 samples with circular cross-sections was collected from the literature [3,21,22,24,33–49].

Funding: This research received no external funding.

Data Availability Statement: The dataset used in this paper is available under the GitHub link https://github.com/ccakiroglu/AFRP (accessed on 27 October 2023).

Conflicts of Interest: The author declares no conflict of interest.

References

1. Green, M.F.; Bisby, L.A.; Fam, A.Z.; Kodur, V.K. FRP confined concrete columns: Behaviour under extreme conditions. *Cem. Concr. Compos.* **2006**, *28*, 928–937. [CrossRef]
2. Parvin, A.; Brighton, D. FRP Composites Strengthening of Concrete Columns under Various Loading Conditions. *Polymers* **2014**, *6*, 1040–1056. [CrossRef]
3. Arabshahi, A.; Gharaei-Moghaddam, N.; Tavakkolizadeh, M. Development of applicable design models for concrete columns confined with aramid fiber reinforced polymer using Multi-Expression Programming. *Structures* **2020**, *23*, 225–244. [CrossRef]
4. Shih, C.-H.; You, J.-L.; Lee, Y.-L.; Cheng, A.-Y.; Chang, C.-P.; Liu, Y.-M.; Ger, M.-D. Design and Ballistic Performance of Hybrid Plates Manufactured from Aramid Composites for Developing Multilayered Armor Systems. *Polymers* **2022**, *14*, 5026. [CrossRef] [PubMed]
5. Alkhatib, F.; Mahdi, E.; Dean, A. Design and Evaluation of Hybrid Composite Plates for Ballistic Protection: Experimental and Numerical Investigations. *Polymers* **2021**, *13*, 1450. [CrossRef]
6. Lee, Y.S.; Wetzel, E.D.; Wagner, N.J. The ballistic impact characteristics of Kevlar® woven fabrics impregnated with a colloidal shear thickening fluid. *J. Mater. Sci.* **2003**, *38*, 2825–2833. [CrossRef]
7. Wang, X.; Zhang, J.; Bao, L.; Yang, W.; Zhou, F.; Liu, W. Enhancement of the ballistic performance of aramid fabric with polyurethane and shear thickening fluid. *Mater. Des.* **2020**, *196*, 109015. [CrossRef]
8. Meliande, N.M.; Oliveira, M.S.; Silveira, P.H.P.M.d.; Dias, R.R.; Marçal, R.L.S.B.; Monteiro, S.N.; Nascimento, L.F.C. Curaua–Aramid Hybrid Laminated Composites for Impact Applications: Flexural, Charpy Impact and Elastic Properties. *Polymers* **2022**, *14*, 3749. [CrossRef]
9. Khedmatgozar Dolati, S.S.; Mehrabi, A. FRP sheet/jacket system as an alternative method for splicing prestressed-precast concrete piles. *Case Stud. Constr. Mater.* **2022**, *16*, e00912. [CrossRef]
10. Khedmatgozar Dolati, S.S.; Mehrabi, A. NSM FRP pile-splice system for prestressed precast concrete piles. *Pract. Period. Struct. Des. Constr.* **2022**, *27*, 04022046. [CrossRef]
11. Tin, H.-X.; Thuy, N.-T.; Seo, S.-Y. Structural Behavior of RC Column Confined by FRP Sheet under Uniaxial and Biaxial Load. *Polymers* **2022**, *14*, 75. [CrossRef] [PubMed]
12. Choi, E.; Jeon, J.S.; Cho, B.S.; Park, K. External jacket of FRP wire for confining concrete and its advantages. *Eng. Struct.* **2013**, *56*, 555–566. [CrossRef]
13. Iacobucci, R.D.; Sheikh, S.A.; Bayrak, O. Retrofit of square concrete columns with carbon fiber-reinforced polymer for seismic resistance. *Struct. J.* **2003**, *100*, 785–794.
14. Yang, H.; Song, H.; Zhang, S. Experimental investigation of the behavior of aramid fiber reinforced polymer confined concrete subjected to high strain-rate compression. *Constr. Build. Mater.* **2015**, *95*, 143–151. [CrossRef]

15. Xie, D.; Hu, Z.; Wang, B.; Zhao, K.; Shi, Y. Axial behavior of basalt FRP-confined reinforced concrete columns with square sections of different corner radii. *Eng. Struct.* **2023**, *274*, 115153. [CrossRef]
16. Sharma, S.S.; Dave, U.V.; Solanki, H. FRP Wrapping for RC Columns with Varying Corner Radii. *Procedia Eng.* **2013**, *51*, 220–229. [CrossRef]
17. Pour, A.F.; Ozbakkaloglu, T.; Vincent, T. Simplified design-oriented axial stress-strain model for FRP-confined normal-and high-strength concrete. *Eng. Struct.* **2018**, *175*, 501–516. [CrossRef]
18. Pham, T.M.; Hadi, M.N. Confinement model for FRP confined normal-and high-strength concrete circular columns. *Constr. Build. Mater.* **2014**, *69*, 83–90. [CrossRef]
19. Lam, L.; Teng, J.G. Design-oriented stress–strain model for FRP-confined concrete. *Constr. Build. Mater.* **2003**, *17*, 471–489. [CrossRef]
20. Wei, Y.Y.; Wu, Y.F. Unified stress–strain model of concrete for FRP-confined columns. *Constr. Build. Mater.* **2012**, *26*, 381–392. [CrossRef]
21. Wu, H.L.; Wang, Y.F.; Yu, L.; Li, X.R. Experimental and computational studies on high-strength concrete circular columns confined by aramid fiber-reinforced polymer sheets. *J. Compos. Constr.* **2009**, *13*, 125–134. [CrossRef]
22. Wang, Y.F.; Wu, H.L. Size effect of concrete short columns confined with aramid FRP jackets. *J. Compos. Constr.* **2010**, *15*, 535–544. [CrossRef]
23. Djafar-Henni, I.; Kassoul, A. Stress–strain model of confined concrete with Aramid FRP wraps. *Constr. Build. Mater.* **2018**, *186*, 1016–1030. [CrossRef]
24. Lobo, P.S.; Faustino, P.; Jesus, M.; Marreiros, R. Design model of concrete for circular columns confined with AFRP. *Compos. Struct.* **2018**, *200*, 69–78. [CrossRef]
25. Song, H.; Ahmad, A.; Farooq, F.; Ostrowski, K.A.; Maślak, M.; Czarnecki, S.; Aslam, F. Predicting the compressive strength of concrete with fly ash admixture using machine learning algorithms. *Constr. Build. Mater.* **2021**, *308*, 125021. [CrossRef]
26. Song, H.; Ahmad, A.; Ostrowski, K.A.; Dudek, M. Analyzing the Compressive Strength of Ceramic Waste-Based Concrete Using Experiment and Artificial Neural Network (ANN) Approach. *Materials* **2021**, *14*, 4518. [CrossRef]
27. Anjum, M.; Khan, K.; Ahmad, W.; Ahmad, A.; Amin, M.N.; Nafees, A. Application of Ensemble Machine Learning Methods to Estimate the Compressive Strength of Fiber-Reinforced Nano-Silica Modified Concrete. *Polymers* **2022**, *14*, 3906. [CrossRef]
28. Ahmad, A.; Ahmad, W.; Aslam, F.; Joyklad, P. Compressive strength prediction of fly ash-based geopolymer concrete via advanced machine learning techniques. *Case Stud. Constr. Mater.* **2022**, *16*, e00840. [CrossRef]
29. Shang, M.; Li, H.; Ahmad, A.; Ahmad, W.; Ostrowski, K.A.; Aslam, F.; Joyklad, P.; Majka, T.M. Predicting the Mechanical Properties of RCA-Based Concrete Using Supervised Machine Learning Algorithms. *Materials* **2022**, *15*, 647. [CrossRef]
30. Ahmad, A.; Chaiyasarn, K.; Farooq, F.; Ahmad, W.; Suparp, S.; Aslam, F. Compressive Strength Prediction via Gene Expression Programming (GEP) and Artificial Neural Network (ANN) for Concrete Containing RCA. *Buildings* **2021**, *11*, 324. [CrossRef]
31. Farooq, F.; Nasir Amin, M.; Khan, K.; Rehan Sadiq, M.; Faisal Javed, M.; Aslam, F.; Alyousef, R. A Comparative Study of Random Forest and Genetic Engineering Programming for the Prediction of Compressive Strength of High Strength Concrete (HSC). *Appl. Sci.* **2020**, *10*, 7330. [CrossRef]
32. Amin, M.N.; Ahmad, A.; Khan, K.; Ahmad, W.; Nazar, S.; Faraz, M.I.; Alabdullah, A.A. Split Tensile Strength Prediction of Recycled Aggregate-Based Sustainable Concrete Using Artificial Intelligence Methods. *Materials* **2022**, *15*, 4296. [CrossRef] [PubMed]
33. Nanni, A.; Bradford, N.M. FRP jacketed concrete under uniaxial compression. *Constr. Build. Mater.* **1995**, *9*, 115–124. [CrossRef]
34. Watanabe, K.; Nakamura, H.; Honda, Y.; Toyoshima, M. Confinement Effect of FRP Sheet on Strength and Ductility of Concrete Cylinders under Uniaxial Compression. In *Non-Metallic (FRP) Reinforcement for Concrete Structures*; Japan Concrete Institute: Tokyo, Japan, 1997; Volume 1, pp. 233–240.
35. Rochette, P.; Labossiere, P. Axial testing of rectangular column models confined with composites. *J. Compos. Constr.* **2000**, *4*, 129–136. [CrossRef]
36. Suter, R.; Pinzelli, R. Confinement of Concrete columns with FRP sheets. In Proceedings of the Fifth International Conference on Fiber Reinforced Plastics for Reinforced Concrete Structures, Cambridge, UK, 16–18 July 2001.
37. Toutanji, H.; Deng, Y. Strength and durability performance of concrete axially loaded members confined with AFRP composite sheets. *Compos. Part B Eng.* **2002**, *33*, 255–261. [CrossRef]
38. Miller, C.; Rohrlach, D.; Staak, A.; Verma, K. Behaviour of Fibre Reinforced Polymer Confined High Strength Concrete under Axial Cyclic Compression. Ph.D. Thesis, The School of Civil, Environmental and Mining Engineering, The University of Adelaide, Adelaide, Australia, 2007.
39. Wu, G.; Wu, Z.S.; Lu, Z.T.; Ando, Y.B. Structural Performance of Concrete Confined with Hybrid FRP Composites. *J. Reinf. Plast. Compos.* **2008**, *27*, 1323–1348. [CrossRef]
40. Wang, G. Compressive Behaviour of Concrete Confined by Aramid FRP Tubes. Master's Thesis, The School of Civil, Environmental and Mining Engineering, The University of Adelaide, Adelaide, Australia, 2008.
41. Wang, Y.; Zhang, D. Creep-effect on mechanical behavior of concrete confined by FRP under axial compression. *J. Eng. Mech.* **2009**, *135*, 1315–1322. [CrossRef]
42. Ozbakkaloglu, T.; Akin, E. Behavior of FRP-confined normal-and high-strength concrete under cyclic axial compression. *J. Compos. Constr.* **2012**, *16*, 451–463. [CrossRef]

43. Dai, J.G.; Bai, Y.L.; Teng, J.G. Behavior and modeling of concrete confined with FRP composites of large deformability. *J. Compos. Constr.* **2011**, *15*, 963–973. [CrossRef]
44. Cheek, J.; Formichella, N.; Graetz, D.; Varasteh, S. The Behavior of Ultra-High Strength Concrete in FRP Confined Concrete Systems under Axial Compression. Bachelor's Thesis, The School of Civil, Environmental and Mining Engineering, The University of Adelaide, Adelaide, Australia, 2011.
45. Vincent, T.; Ozbakkaloglu, T. Influence of fiber orientation and specimen end condition on axial compressive behavior of FRP-confined concrete. *Constr. Build. Mater.* **2013**, *47*, 814–826. [CrossRef]
46. Ozbakkaloglu, T.; Vincent, T. Axial compressive behavior of circular high-strength concrete-filled FRP tubes. *J. Compos. Constr.* **2014**, *18*, 04013037. [CrossRef]
47. Ozbakkaloglu, T. Compressive behavior of concrete-filled FRP tube columns: Assessment of critical column parameters. *Eng. Struct.* **2013**, *51*, 188–199. [CrossRef]
48. Vincent, T.; Ozbakkaloglu, T. Influence of slenderness on stress-strain behavior of concrete-filled FRP tubes: Experimental study. *J. Compos. Constr.* **2015**, *19*, 04014029. [CrossRef]
49. Lim, J.C.; Ozbakkaloglu, T. Hoop strains in FRP-confined concrete columns: Experimental observations. *Mater Struct* **2015**, *48*, 2839–2854. [CrossRef]
50. Fekri, M.N.; Ghosh, A.M.; Grolinger, K. Generating Energy Data for Machine Learning with Recurrent Generative Adversarial Networks. *Energies* **2020**, *13*, 130. [CrossRef]
51. Marani, A.; Nehdi, M.L. Predicting shear strength of FRP-reinforced concrete beams using novel synthetic data driven deep learning. *Eng. Struct.* **2022**, *257*, 114083. [CrossRef]
52. Goodfellow, I.; Pouget-Abadie, J.; Mirza, M.; Xu, B.; Warde-Farley, D.; Ozair, S.; Courville, A.; Bengio, Y. Generative Adversarial Nets. In Proceedings of the Advances in Neural Information Processing Systems 27 (NIPS 2014), Montreal, QC, Canada, 8–13 December 2014.
53. Xu, L.; Skoularidou, M.; Cuesta-Infante, A.; Veeramachaneni, K. Modeling Tabular data using Conditional GAN. In Proceedings of the Advances in Neural Information Processing Systems 32 (NeurIPS 2019), Vancouver, ON, Canada, 8–14 December 2019.
54. Cakiroglu, C.; Shahjalal, M.; Islam, K.; Mahmood, S.F.; Billah, A.M.; Nehdi, M.L. Explainable ensemble learning data-driven modeling of mechanical properties of fiber-reinforced rubberized recycled aggregate concrete. *J. Build. Eng.* **2023**, *76*, 107279. [CrossRef]
55. Mangalathu, S.; Karthikeyan, K.; Feng, D.C.; Jeon, J.S. Machine-learning interpretability techniques for seismic performance assessment of infrastructure systems. *Eng. Struct.* **2022**, *250*, 112883. [CrossRef]
56. Somala, S.N.; Chanda, S.; Karthikeyan, K.; Mangalathu, S. Explainable Machine learning on New Zealand strong motion for PGV and PGA. *Structures* **2021**, *34*, 4977–4985. [CrossRef]
57. Mangalathu, S.; Hwang, S.H.; Jeon, J.S. Failure mode and effects analysis of RC members based on machine-learning-based SHapley Additive exPlanations (SHAP) approach. *Eng. Struct.* **2020**, *219*, 110927. [CrossRef]
58. Feng, D.C.; Wang, W.J.; Mangalathu, S.; Taciroglu, E. Interpretable XGBoost-SHAP machine-learning model for shear strength prediction of squat RC walls. *J. Struct. Eng.* **2021**, *147*, 04021173. [CrossRef]
59. Wakjira, T.G.; Rahmzadeh, A.; Alam, M.S.; Tremblay, R. Explainable machine learning based efficient prediction tool for lateral cyclic response of post-tensioned base rocking steel bridge piers. *Structures* **2022**, *44*, 947–964. [CrossRef]
60. Lundberg, S.M.; Lee, S.-I. A unified approach to interpreting model predictions. In Proceedings of the 31st Conference on 577 Neural Information Processing Systems (NIPS 2017), Long Beach, CA, USA, 4–9 December 2017.